Journal of Biomedical Optics

BiomedicalOptics.SPIEDigitalLibrary.org

Review of methods and applications of attenuation coefficient measurements with optical coherence tomography

Shuang Chang
Audrey K. Bowden

SPIE.

Shuang Chang, Audrey K. Bowden, "Review of methods and applications of attenuation coefficient measurements with optical coherence tomography," *J. Biomed. Opt.* **24**(9), 090901 (2019), doi: 10.1117/1.JBO.24.9.090901.

Journal of Biomedical Optics 24(9), 090901 (September 2019)

REVIEW

Review of methods and applications of attenuation coefficient measurements with optical coherence tomography

Shuang Chang and Audrey K. Bowden*
Vanderbilt University, Vanderbilt Biophotonics Center, Department of Biomedical Engineering, Nashville, Tennessee, United States

Abstract. The optical attenuation coefficient (AC), an important tissue parameter that measures how quickly incident light is attenuated when passing through a medium, has been shown to enable quantitative analysis of tissue properties from optical coherence tomography (OCT) signals. Successful extraction of this parameter would facilitate tissue differentiation and enhance the diagnostic value of OCT. In this review, we discuss the physical and mathematical basis of AC extraction from OCT data, including current approaches used in modeling light scattering in tissue and in AC estimation. We also report on demonstrated clinical applications of the AC, such as for atherosclerotic tissue characterization, malignant lesion detection, and brain injury visualization. With current studies showing AC analysis as a promising technique, further efforts in the development of methods to accurately extract the AC and to explore its potential use for more extensive clinical applications are desired. [DOI: 10.1117/1.JBO.24.9.090901]

Keywords: light attenuation coefficient; optical coherence tomography; tissue differentiation.

Paper 190161VR received May 16, 2019; accepted for publication Aug. 16, 2019; published online Sep. 13, 2019.

1 Introduction

Optical coherence tomography (OCT) is an established technique that provides noninvasive, volumetric, and real-time *in vivo* images of tissue microstructure.[1] One longstanding criticism of traditional OCT images (i.e., B-scans), however, is that they only provide morphological information about the tissue.[2,3] Quantitative analysis of tissue properties would facilitate more accurate differentiation between diseased tissue and normal tissue. Several researchers have proposed that the optical attenuation coefficient (AC), which measures how quickly incident light is attenuated when passing through a medium, may enable such analysis. Indeed, analysis of the AC has been used for quantitative assessment and differentiation of several tissue types:[4] for example, quantification of the AC from OCT data enables *in vivo* diagnostic applications, such as imaging of atherosclerotic plaques,[3] assessment of glaucoma,[5] identification of axillary lymph nodes,[6] differentiation between normal and cancerous tissue in the bladder[7] and colon,[8] and imaging of the cerebral cortex after stroke.[9] In addition, measurement of the AC also serves to assess vascularity in human burn scars[10] and development of acne scars,[11] as well as to monitor the effect of photodynamic therapy in skin lesions.[12]

The purpose of this review is to discuss the physical and mathematical basis that underlies extraction of the AC from OCT data and present a summary of demonstrated clinical applications of the OCT-derived AC, as well as a historical perspective, contemporary assessment, and futuristic outlook on methods used to estimate the AC with OCT. Our chief aim is that readers gain an appreciation for the importance, complexity, and applicability of this parameter, as well an appreciation of the tradeoffs of different implementations, in order to guide decisions about how to employ it for analysis of their clinical datasets.

We begin with some background of principles of OCT measurement and a definition of the AC. Then, we discuss relevant mathematical models, methods, and clinical applications of the AC.

2 Background

2.1 *Principle of OCT*

The general strategy for implementing OCT is based on low-coherence interferometry. Traditionally, infrared light of low temporal coherence is used to illuminate the tissue; the choice of wavelength depends on the type of tissue being illuminated and is largely governed by the goal to minimize loss of signal due to absorption. Light incident on the tissue of interest is collected in a backscattering geometry and mixed with light returning from a reference path. The resulting signal is presented in the form of an axial scan (A-scan), which describes the relative position and intensity of reflecting structures (corresponding to interfaces of different cell or tissue properties) in the tissue. Thus, OCT provides a profile of the underlying tissue microstructure. A spatial series of A-scans form a two-dimensional dataset and create a cross-sectional image, termed a B-scan.

The maximum depth into tissue that an A-scan can measure is governed by at least three factors. First, the optics of the system affect how light is distributed to different tissue depths: the maximum concentration of illuminating light will occur at the focus of the objective and will taper as one moves deeper into the tissue. The shape of this focusing profile is determined by the confocal function of the system. Second, Fourier-domain OCT systems,[13] which are more popular than their time-domain counterparts, have a maximum imaging depth determined by the sampling frequency and subject to the Nyquist sampling limit.

*Address all correspondence to Audrey K. Bowden, E-mail: a.bowden@vanderbilt.edu

Most researchers, however, typically choose the optics and design of their system, such that the imaging depth of most OCT systems is practically limited by a third factor, which is light attenuation by the tissue.

2.2 *Principle of AC*

The AC measures how quickly incident light is attenuated when passing through a medium and is a function of the underlying medium properties. Loss of light in tissue can be caused by absorption, scattering, or a combination of both. When propagating through a medium, the irradiance of the light beam follows the equation:

$$I = I_0 e^{-\mu z}, \tag{1}$$

where z is the distance light travels into tissue and μ is the AC of light in that tissue. When μ is small, the irradiance of light will experience a slow exponential decay, as happens when the tissue sample has low absorption and weakly scattering properties. In contrast, when μ is large, the irradiance will decrease quickly and exponentially, as happens in highly scattering or absorbing tissue types. Because AC is an underlying tissue property, accurate estimation of the AC allows differentiation of dissimilar tissue types. This information is complementary to information about the tissue microstructure provided by standard OCT B-scans, which represents the backscatter intensity at each depth. In fact, a true picture of the backscatter intensity at each depth should take into account the fact that the light incident at each depth of the tissue is reduced by attenuation of light from anterior structures. Figure 1 shows a conventional OCT B-scan of a healthy human retina compared to AC mapping. Note that to some degree, the intensity of scattering correlates with the magnitude of the AC, as one would expect.

2.3 *Models for AC Extraction*

Multiple methods have been proposed to extract AC measurements from OCT images. These methods are associated with two general models that have been proposed: the single-scattering (SS) model[15,16] and the multiple-scattering (MS) model[17] and the tissue type of interest determines which model should be used. The SS model assumes the backscattering of photons only occurs once and is applicable to AC measurement in weakly scattering tissue samples or superficial layers of a highly scattering tissue sample, such as human axillary lymph nodes[6] and the retinal nerve fiber layer (RNFL).[5] The MS model takes multiple backscattering events and larger probing depths[18] into consideration, and it has been used for extracting optical properties from human skin[19] and blood vessels.[20] The SS model is more widely used, especially as SS is a general assumption of OCT image reconstruction.

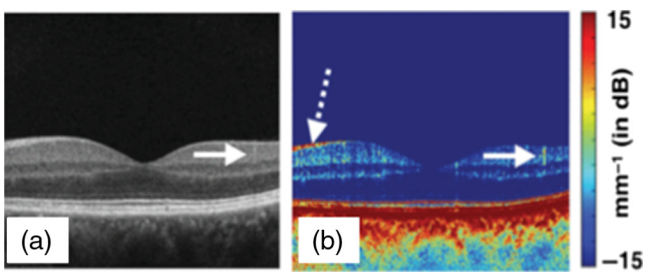

Fig. 1 (a) Images of human retina obtained by commercialized OCT (a) in comparison with AC mapping. Dashed arrow in (b) points to the RNFL of the retina. Solid arrows in (a) and (b) point to a shadow resulting from a superficial retinal blood vessel (reprinted with permission from Ref. 14).

2.3.1 *Single-scattering model*

Within the SS model, two main approaches have been described, which are known as curve-fitting (CF) and depth-resolved (DR),[15,16] respectively. The general idea behind CF methods is to fit the exponential decay described by Eq. (1) to the A-scan data of interest and determine the AC as the exponential parameter that best fits this curve. In contrast, DR methods use differences in the intensity of adjacent voxels to recover the amount of attenuation that occurs on a per-pixel basis. Historically, CF methods were the first to be introduced, and the majority of OCT literature on the AC still relies on this method. However, the use of DR methods, first introduced in 2014,[15] is increasing as attempts to streamline and automate the process of AC extraction become popular.

While these two methods have been successful, the utility of the AC for clinical diagnoses has inspired many recent works that are dedicated to improving their performance. For example, van Soest et al. developed an automated optimization-based CF method, with the assumption that the region of interest is homogenous.[21] Gargesha et al. employed a three-dimensional approach, where groups of A-lines with close proximity were analyzed together, as opposed to single A-line analysis, to extract AC values from atherosclerotic tissue.[22] Smith et al. modified the DR method to take the confocal function into account (DRC), which allows the focal plane to be placed within the sample.[23] Dwork et al. introduced an automated DRC algorithm, which computes the AC at each pixel without requiring prior knowledge of the OCT system parameters.[14] We next review the basic mathematical models associated with the two SS methods and overview the innovations that have been recently developed.

CF method. An early approach used to measure the optical AC relies on a simplified model in which either an exponential curve is fit to a one-dimensional OCT signal (A-scan) or a linear function is fit to the logarithm of that signal; a nonlinear least square fitting is then invoked to find the estimated values.[16] A limitation with this classical CF approach is that it requires taking the average over a large amount of measured data points to obtain reliable estimations from fitting the exponential curve, and therefore, only relatively global AC measurements can be achieved.

a. General CF method

The CF method was first introduced by Faber et al.[16] The detected OCT signal is purported to follow the Lambert–Beer's law shown in Eq. (1). In order to accurately extract AC values, Faber et al. also take the effect of the confocal point spread function into consideration by introducing the following expression:

$$h(z) = \left(\left(\frac{z - z_{cf}}{z_R}\right)^2 + 1\right)^{-1}, \tag{2}$$

where h is the confocal function, z_{cf} denotes the focal plane depth, and z_R is the apparent Rayleigh range. The term z_R is

defined as $z_R = \alpha n z_r$, where $\alpha = 2$ for diffuse reflection ($\alpha = 1$ for specular reflection), n is the index of refraction of the tissue sample, and z_r is the Rayleigh range of the scanning lens. Faber showed that when the focal plane of the optical system is located within the sample, the confocal function needs to be taken into account in order to best describe the resulting OCT signal. Therefore, by combining Eqs. (1) and (2), Faber concludes that the recorded OCT signal intensity can be modeled as

$$I(z) \propto h(z)e^{-2\mu z}, \tag{3}$$

where the factor of 2 accounts for the light being attenuated twice due to the round-trip backscattering event measured with OCT. The estimated AC (μ) in a given medium can then be found by fitting the averaged OCT A-scans to the model described in Eq. (3). The CF algorithm used in Faber's method finds the maximum likelihood estimation by minimizing χ^2, which is given by

$$\chi^2 = \sum_{i=1}^{N} \left(\frac{y_i - f(x_i; a_1 \ldots a_M)}{\sigma_i} \right)^2, \tag{4}$$

where y_i are the recorded intensities, x_i are depths, f is the model written in Eq. (2), and a_j are the fitted parameters to be determined [in this case, the fitted parameters are μ and a multiplier A to Eq. (2)]. An example of an application of the CF method is shown in Fig. 2, where different types of atherosclerotic tissue can be differentiated[3] on the basis of different attenuations.

b. CF with a reference layer

Vermeer et al.[24] applied and updated Faber's CF method for extraction of the AC in the RNFL of the eye by using the retinal pigment epithelium (RPE) as a reference layer to normalize the OCT data. The reason for normalization is that before reaching the retina, the incident light is first attenuated by the anterior segment and the vitreous region of the eye, so the power of light that reaches the top layer of the retina (RNFL) is already a fraction of the initial incident light power. In essence, they recognized that the total power incident on the retina fluctuates due to the differences in opacity and the amount of vitreous humor the light must travel through (i.e., different positions on the retina).

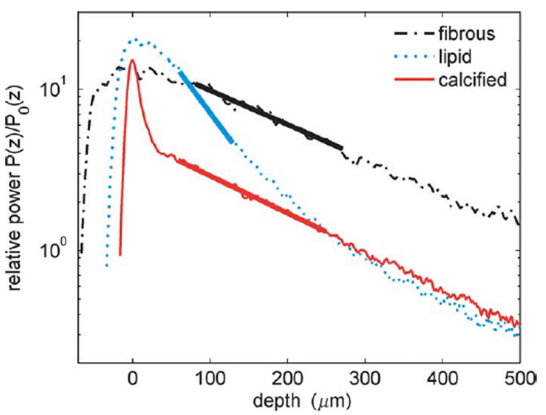

Fig. 2 CF method applied to *ex vivo* atherosclerotic plaque characterization, where thick lines show the fitting over areas of interest (reprinted with permission from Ref. 3).

Because the RPE is another highly scattering layer in the retina that is assumed to be uniformly scattering, it was chosen as a reference to normalize the total OCT signal of the RNFL.

The referenced CF method can be understood in the following way. According to Lambert–Beer's law, the differential equation for an attenuated light beam is given by[24]

$$dI(z) = -\mu(z)I(z)\mathrm{d}z, \tag{5}$$

which makes μ a depth-dependent AC and establishes a linear relationship between the incident light intensity and the attenuated light intensity. The power of incident light at depth z into the medium can be expressed as $I(z) = I_0 e^{-\mu z}$, where μ is the AC specific to the medium. The backscattered light is a fraction of the attenuated light, which has a power of $\alpha\mu I_0 e^{-\mu z}$ at depth z and a power of $\alpha\mu I_0 e^{-2\mu z}$ at the detector. The additional factor of 2 accounts for the roundtrip attenuation.

By integrating over a depth range d, the total power of backscattered light from this depth range can be expressed as

$$S = \int_{z=0}^{d} \gamma\alpha\mu I_0 e^{-2\mu z}\mathrm{d}z = \frac{\gamma\alpha I_0}{2}(1 - e^{-2\mu d}), \tag{6}$$

where S is the total OCT signal, I_0 is the incident light intensity, γ is the conversion factor that converts the detected backscattered OCT signal to digital signal, and α is the fraction of light arriving at the layer of interest. Therefore, the total OCT signal backscattered from the RNFL is given by $S_{\mathrm{RNFL}} = \frac{\gamma\alpha_{\mathrm{RNFL}} I_0}{2}(1 - e^{-2\mu_{\mathrm{RNFL}} d_{\mathrm{RNFL}}})$, and the total OCT signal reflecting from the RPE layer is $S_{\mathrm{RPE}} = \frac{\gamma\alpha_{\mathrm{RPE}} I_0}{2}(1 - e^{-2\mu_{\mathrm{RPE}} d_{\mathrm{RPE}}}) e^{-2\mu_{\mathrm{RNFL}} d_{\mathrm{RNFL}}}$, assuming the intensity loss between the RNFL and RPE layers is negligible. Then, Vermeer et al. compute the ratio R of the total signal in the RNFL over the total signal in the RPE:

$$R = \frac{S_{\mathrm{RNFL}}}{S_{\mathrm{RPE}}} = \frac{\frac{\gamma\alpha_{\mathrm{RNFL}} I_0}{2}(1 - e^{-2\mu_{\mathrm{RNFL}} d_{\mathrm{RNFL}}})}{\frac{\gamma\alpha_{\mathrm{RPE}} I_0}{2}(1 - e^{-2\mu_{\mathrm{RPE}} d_{\mathrm{RPE}}}) e^{-2\mu_{\mathrm{RNFL}} d_{\mathrm{RNFL}}}}$$
$$= \frac{\alpha_{\mathrm{RNFL}}(e^{2\mu_{\mathrm{RNFL}} d_{\mathrm{RNFL}}} - 1)}{\alpha_{\mathrm{RPE}}(1 - e^{-2\mu_{\mathrm{RPE}} d_{\mathrm{RPE}}})}. \tag{7}$$

Because the author assumes that the attenuation in the RPE and the thickness of the RPE, d_{RPE}, are constant for a given person, the above expression can be simplified to

$$R = \beta(e^{2\mu_{\mathrm{RNFL}} d_{\mathrm{RNFL}}} - 1), \tag{8}$$

where β is a constant and equals $\frac{\alpha_{\mathrm{RNFL}}}{\alpha_{\mathrm{RPE}}(1 - e^{-2\mu_{\mathrm{RPE}} d_{\mathrm{RPE}}})}$. Then β and μ_{RNFL} can be estimated by fitting the model to the ratio R determined from intensity measurements, and the optimal fit is found by minimizing the error defined by the L^1-norm of the difference between the model and the actual data:

$$\{\beta, \mu\} = \arg\min_{\beta,\mu} \sum_i \left| \log\left(\frac{\beta(e^{2\mu d_i} - 1)}{R_i} \right) \right| \tag{9}$$

With known β, the attenuation of the RNFL layer can be solved as follows:

$$\mu_{\mathrm{RNFL}} = \frac{\log\left(\frac{R}{\beta} + 1\right)}{2d_{\mathrm{RNFL}}}. \tag{10}$$

This work underscores the importance of understanding the physiology of the underlying tissue to extract meaningful measurements of the AC.

DR method. As previously mentioned, one drawback of the CF method is that a large amount of data is needed to accurately fit a curve, leading to an inability to extract values over small tissue regions. In the past few years, however, new approaches have emerged for extracting AC that offer higher resolution than CF. For example, the DR model developed by Vermeer et al.[15] in 2014 allows for estimation of the AC for each pixel, which enables pixelwise tissue-type differentiation in both homogeneous and heterogeneous tissues. This is in contrast to the CF method, which only works with a single, uniform tissue type or requires an additional step of segmenting the tissue manually or using automated methods.[15,16]

a. General DR method

The DR method relies on two fundamental assumptions: first, light is attenuated almost completely within the measured imaging depth range; second, the fraction of backscattered light collected by the photodetector of the OCT system from the attenuated light is a constant.[15] Note that the latter assumption may not be true in the case of significant attenuation due to absorption. Vermeer's method enables pixelwise estimation of the OCT data, and this is also based on the SS model. According to the linear relationship between the incident light intensity and the attenuated light intensity in Eq. (5), at the zero-depth condition ($z = 0$, boundary condition), Eq. (5) can be solved as follows:

$$L(z) = I_0 e^{-\int_0^z \mu(u)\mathrm{d}u}, \tag{11}$$

where $L(z)$ is the attenuated light intensity at depth z and the incident light intensity is given by I_0. The actual detected OCT signal can be expressed in Eq. (12):

$$I(z) = A\kappa\mu(z) I_0 e^{-2\int_0^z \mu(u)\mathrm{d}u}, \tag{12}$$

where the factor 2 accounts for the round-trip attenuation of light in tissue, A is the constant ratio of backscattered light to total attenuated light, and κ is the conversion factor during digitizing and integrating of the signal. Then, the AC in a given region of the medium can be estimated by solving for $\mu(z)$ with a depth range D:

$$\mu(z) \approx \frac{I(z)}{2\int_z^D I(u)\mathrm{d}u}. \tag{13}$$

Equation (13) allows the definition of AC on a continuous domain, so if a pixelwise coefficient value is desired, then the intensity measurements need to be integrated and averaged over the pixel size Δ, which is commonly related to the coherence length of the light source. When the integral is solved for each pixel, the expression can be written as: $\mu[i] = \frac{1}{2\Delta}\log\left(1 + \frac{I[i]}{\sum_{i+1}^{\infty} I[i]}\right)$. Simplifying the $\log(1+x)$ term with a first-order linearization, which is equivalent to x assuming x is small, the expression can be rewritten as

$$\mu[i] \approx \frac{I[i]}{2\Delta\sum_{i+1}^{\infty} I[i]}. \tag{14}$$

Vermeer's DR method improves estimation of the AC in that it does not require fitting a curve to OCT signals, which may be affected by noise in the data. Pixelwise estimation enables application on multilayered tissues, as shown in Fig. 3, and because this method compares the local OCT signal to the integral of signals from deeper layers, it allows accurate estimation from thin or superficial layers.

Sensitivity fall-off is a phenomenon that affects the perceived OCT intensity in SD-OCT systems. This phenomenon leads to a decrease of system sensitivity with depth due to the greater reduction of fringe visibility by the finite resolution of the spectrometer at higher fringe frequencies.[25] The effect caused by this sensitivity decay was also considered in Vermeer's method, where they employ a Gaussian model of imaging depth z and width σ:

$$S(z) = e^{\frac{-z^2}{\sigma^2}}, \tag{15}$$

where the width of the Gaussian model σ can be determined from sensitivity measurements. Vermeer's group corrects this fall-off effect by dividing each A-line measurement by this sensitivity factor $S(z)$.

One limitation of the classical DR method is that it does not take the confocal function into consideration. In low AC regions, the dependency on the confocal function is significant.

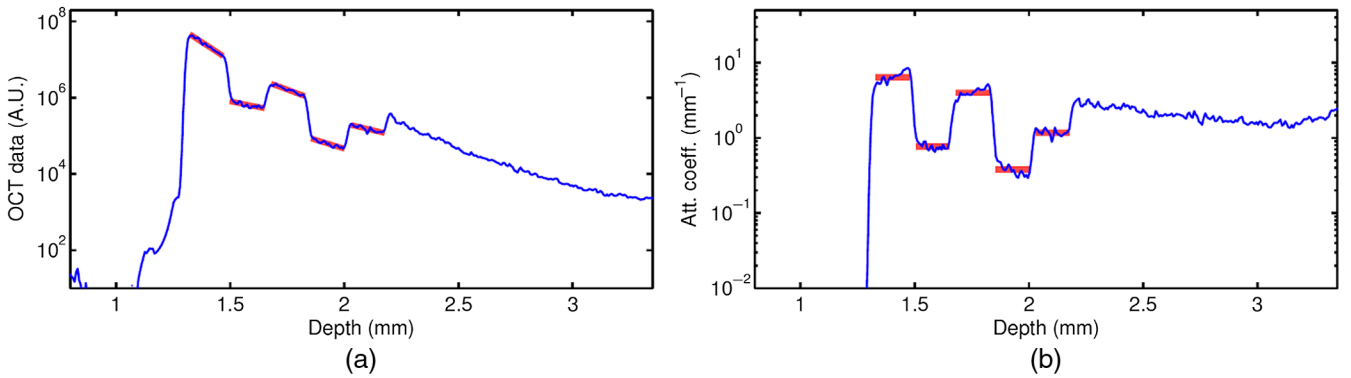

Fig. 3 (a) Depth profile (A-scan) of a layered phantom and (b) the pixelwise attenuation estimated using the DR method. With DR estimation, pixel-specific AC measurement can be achieved. Thick red lines indicate depth ranges, where measurements were taken (reprinted with permission from Ref. 15).

Vermeer et al. circumvent the need to account for confocal parameters in their algorithm by placing the focal plane above the sample (i.e., with the effect of forcing the region of interest to be acquired in a domain where the confocal function is almost constant), but this leads to overestimation in low-attenuation regions.

b. DR confocal

In 2016, Smith et al. introduced a modification of the DR method, termed the depth-resolved confocal (DRC) method that accounts for both the confocal function $h(z)$ and sensitivity fall-off effect in processing the OCT signal.[23] The DRC method addresses the issue with the DR method that accurate ACs can only be extracted when the focal plane is not located in the tissue sample, a condition that does not hold true for many common clinical applications and also leads to reduced signal-to-noise ratio (SNR).[15] With DRC, AC can be extracted while the focal plane is placed within the sample.

In Smith's work, a more comprehensive sensitivity fall-off model[25] is used, allowing more accurate estimation of AC to be extracted than the Gaussian model used by Vermeer's DR method. The comprehensive model accounting for the sensitivity fall-off effect used in Smith's paper is expressed as $S(z)$:

$$S(z) = \left(\frac{\sin\zeta}{\zeta}\right)^2 \cdot \exp\left(-\frac{\left(\frac{\delta\lambda}{\Delta\lambda}\right)^2}{2\ln 2}\zeta^2\right). \tag{16}$$

In this model, $S(z)$ is the magnitude of signal decay and $\zeta = \frac{\pi \cdot z}{2 \cdot z_{RD}}$ describes the depth z, normalized by the maximum ranging depth z_{RD}, which is equal to $\frac{\lambda_0^2}{4\Delta\lambda}$, where λ_0 is the central wavelength of the light source, $\Delta\lambda$ is the wavelength spacing between pixels, and $\delta\lambda$ is spectral resolution of spectrometer (FWHM). By combining Eqs. (2), (12), and (16), the final light attenuation model used in Smith's work becomes

$$I_{fh}(z) = S(z)h(z)\kappa L_0 \alpha\mu(z)e^{-2\int_0^z \mu(\theta)\mathrm{d}\theta}, \tag{17}$$

where the confocal function $h(z)$ is determined experimentally with known locations of the focal plane and the Rayleigh range of OCT system, and the parameters of the sensitivity fall-off function were determined by imaging a neural density filter and fitting the data to Eq. (15). Bilayer simulation results comparing the performance of DRC and DR are shown in Fig. 4. With the updates Smith et al. made in DRC, AC measurement can be extracted without restrictions on focal plane position, which permits imaging with enhanced SNR and enables AC measurement for a wider range of clinical applications.

c. Optimized depth-resolved estimation

Liu et al. address another assumption made in Vermeer's method,[26] which is that all light is attenuated at the bottom of the image range [i.e., boundary condition $\mathrm{I}(\infty) = 0$]. Notably, this assumption may fail in cases, where the light does not completely decay at the penetration depth. In Vermeer's paper, this infinite detection depth is replaced with a limited depth range N, and $\sum_{i=z+1}^{N} I[i] \approx \sum_{i=z+1}^{\infty} I[i]$. While this approximation works for small depths z, issues arise when the imaging depth increases, leading to an increasing difference between $\sum_{i=z+1}^{N} I[i]$ and $\sum_{i=z+1}^{\infty} I[i]$. This estimation error is greatest at $z = N - 1$. Liu et al. recently developed an optimized depth-resolved estimation (ODRE) method to minimize this error. In their method, they rewrite the attenuation equation at the last data point $z = N$ as follows:

$$\begin{aligned}\mu[z] &= \frac{I[z]}{2\Delta\sum_{i=z+1}^{N} I[i] + 2\Delta\sum_{i=z+1}^{\infty} I[i]} \\ &= \frac{I[z]}{2\Delta\sum_{i=z+1}^{N} I[i] + \frac{I[N]}{\mu[N]}},\end{aligned} \tag{18}$$

where $\mu[N]$ is unknown and the best approximation of $\mu[N]$ can be determined using exponential CF. From their numerical simulation in Fig. 5, the error associated with increasing depth, which is apparent in conventional DR results, is eliminated

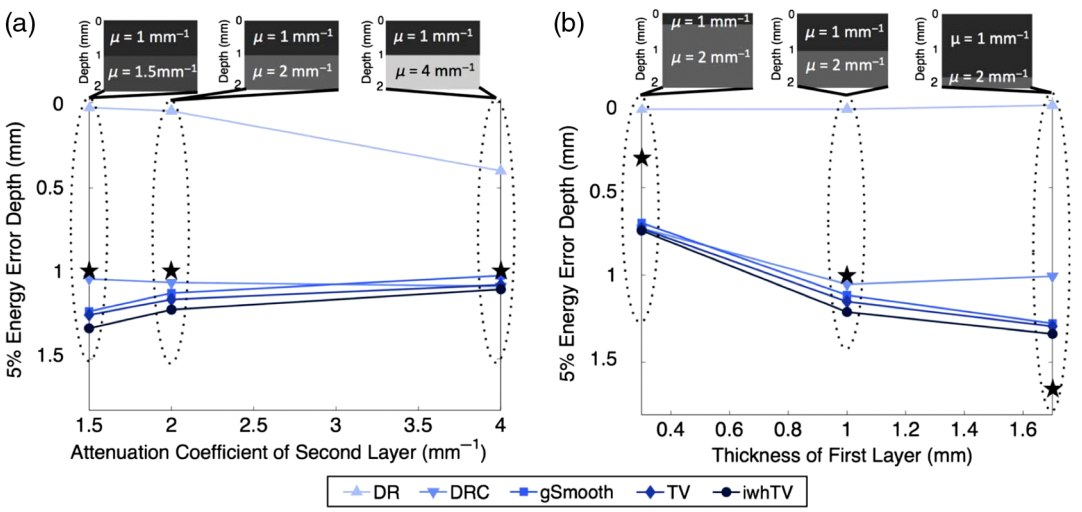

Fig. 4 Simulation results of the effect of (a) AC contrast and (b) layer thickness on DR, DRC, and DRC with various filters [gSmooth, total variance (TV), and intensity weighted horizontal total variation (iwhTV) denoising]. The energy error depth figure of merit is defined as the depth at which the excess energy exceeds 5%; hence, larger energy error depth equates to better performance. Stars indicate positions of the boundary between the layers. From the results, it is evident that DRC outperforms DR with and without denoising (reprinted with permission from Ref. 23).

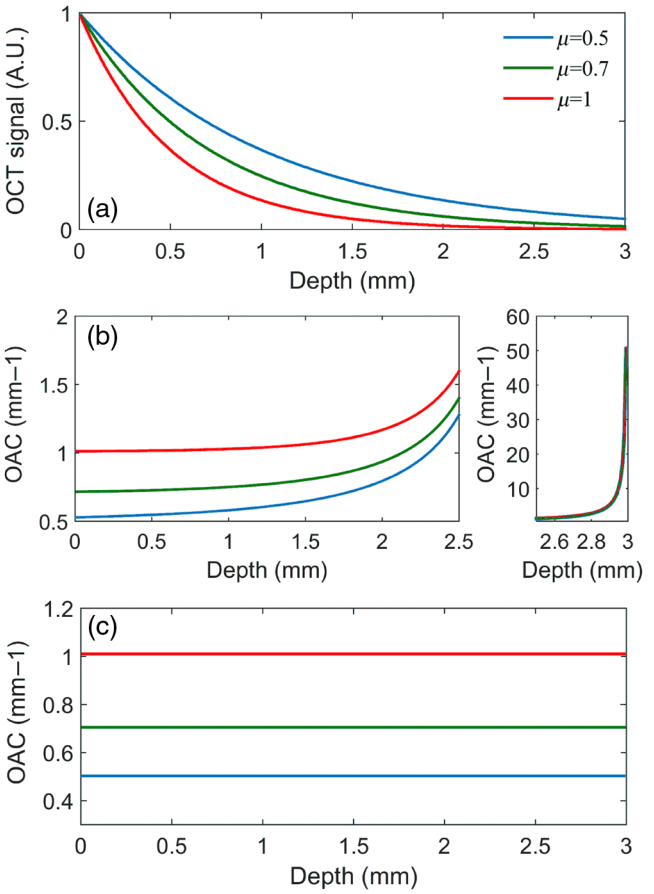

Fig. 5 Numerical simulation of attenuation in a single-layer phantom with homogeneous scattering under noiseless conditions. Note the light does not fully attenuate at the end of the depth region. (a) Simulation OCT signals for varying scattering coefficients. (b) Plot of attenuation versus depth using the DR method; the small graph to the right highlights the large error over the depth range of 2.5 to 3 mm. (c) Plot of attenuation versus depth using the ODRE method shows constant attenuation for all depths, as expected (reprinted with permission from Ref. 26).

using the ODRE method. The difference in the estimation results using the two methods is due to the assumption made in the DR algorithm, which is that all light is attenuated within the depth range of the image. Liu et al. have demonstrated that when light is not fully attenuated, the assumption of the DR method is violated, which causes the estimation error to peak at the bottom of the image, as shown in Fig. 5(b). This is a flaw of the DR algorithm that is corrected by ODRE. In ODRE, the error is minimized, as shown in Fig. 5(c), by approximating $\mu[N]$ with fitting an exponential curve at the last 120 pixels of an averaged A-scan.

2.3.2 *Multiple-scattering model*

In 2015, Almasian et al. developed a comprehensive model for OCT signal analysis that considered effects of both MS and concentration-dependent scattering, as well as system parameters including the confocal point spread function and sensitivity fall-off.[17] For weakly scattering samples, the total AC of OCT signals μ_t equals the sum of the scattering coefficient μ_S and absorption coefficient μ_A, because the effect of multiple-scattered light is negligible. Therefore, the expression can be simplified as: $\mu_t = \mu_S + \mu_A$. However, in situations of samples with a high scattering coefficient and forwardly directed scattering, the effect of MS in OCT signals needs to be considered, as MS leads to a decreased AC: $\mu_t < \mu_S + \mu_A$. In their paper, Almasian et al. proposed the following expression and included the mapping function $f_{NA,g}$:

$$\mu_t = f_{NA,g}(\mu_S) + \mu_A, \tag{19}$$

where g is the scattering anisotropy ($g \approx 1$ for MS). The MS mapping function is dependent on properties of both the confocal function and the angular scattering of the sample.

The author based the analysis of the MS effect on the extended Huygens–Fresnel (EHF) model introduced by Thrane et al.[18] In the EHF model, there are three terms contributing to the mean squared OCT signal $A^2(z)$, which are the single backscattered field, the multiple scattered field, and a coherent cross of the two fields:

$$\langle A^2(z)\rangle \propto e^{-2\mu_S z} + \frac{2e^{-\mu_s z}[1-e^{-\mu_S z}]}{1+\frac{w_S^2(z)}{w_H^2(z)}} + [1-e^{-\mu_S z}]^2 \frac{w_S^2(z)}{w_H^2(z)}. \tag{20}$$

In Eq. (20), $w_H^2(z)$ is the square of the local beam waist of the single backscattered beam and $w_S^2(z)$ is the square of the local beam waist when multiple forward scattering. By substituting $\Delta z = z - z_0$, the expression for $w_H^2(z)$ becomes

$$w_H^2(\Delta z) = w_0^2\left[\left(\frac{z-z_f}{2nZ_{RO}}\right)^2 + 1\right], \tag{21}$$

where w_0^2 is the square of the beam waist measured at the focus in air, z_f is the depth position of the focus, and $Z_{RO} = \pi w_0^2/\lambda_0$ with λ_0 being the center wavelength of the light source. The term $w_S^2(z)$ can be expressed as follows:

$$w_S^2(\Delta z) = w_H^2(\Delta z) + \frac{1}{3}(\mu_S \Delta z)\theta_{\text{rms}}^2 \frac{\Delta z}{n}, \tag{22}$$

where θ_{rms} is the root-mean-square scattering angle describing the angular distribution of the scattered light.

In an MS situation, the confocal point spread function $h(z-z_f)$ and sensitivity fall-off $S(z)$ effects can also be taken into consideration. The confocal PSF can be expressed as follows:

$$h(z-z_f) = \frac{1}{\left(\frac{z-z_f}{2nZ_{RO}}\right)^2 + 1}, \tag{23}$$

where n is the refractive index of the medium in which the measurement is taking place. The sensitivity fall-off effect can be modeled as in Ref. 17:

$$S(z) = \left[\frac{\sin(0.5\Delta k_{\text{sampling}} z)}{0.5\Delta k_{\text{sampling}} z}\right]^2 e^{-\frac{\Delta k_{\text{optical}}^2 z^2}{8\ln 2}}, \tag{24}$$

where the sampling resolution $\Delta k_{\text{sampling}}$ equals the difference between the maximum and minimum wavenumbers of the spectrometer or swept source divided by the number of pixels per spectrum. The value of $\Delta k_{\text{optical}}$ is dependent on the system type. In swept-source OCT, $\Delta k_{\text{optical}}$ equals the instantaneous linewidth of the source, and in spectrometer-OCT systems,

$\Delta k_{optical}$ can be determined from the dispersion linewidth of the spectrometer.

2.3.3 *Model selection for calculating AC in tissues*

In order to accurately determine tissue properties, it is important to know which model, SS or MS, is more appropriate for the tissue of interest. One can determine if a sample should fall under one or the other of the two assumptions quantitatively by calculating the "structure factor," such as the structure factor for discrete random media using the Percus–Yevick equation.[15] Errors will arise if models are inappropriately chosen for analysis: for example, when the MS model is used to analyze results from a weakly scattering tissue, then it is likely that the resulting AC is underestimated. Such errors may lead to misinterpretation of clinical results or unsuccessful differentiation of dissimilar tissue types. Currently, both SS and MS models have been used for analysis in a broad range of clinical applications; however, SS is more often applied due to its simplicity and hence, a greater number of AC extraction algorithms are devoted to SS model.

Compared to the MS model, the SS model has the key advantage of simplicity. As a result, multiple efforts have been made to improve the accuracy of the SS model, and it has been widely used in clinical applications. Careful selection of the SS model algorithms is critical and should be based on biological characteristics of the tissue of interest. In the conventional CF method, several A-scans are averaged for AC extraction; therefore, this method is most suitable for use on homogenous tissue regions and on tissue layers with known segmentation.[16,22] The CF with a reference layer approach by Vermeer et al. demonstrates the importance of understanding the tissue structures and properties prior to AC extraction, as such it can be applied to AC extractions from retinal layers or other layered tissues with a reference layer of relatively constant thickness for normalization.[27] Given that an exponential curve is fitted through a depth range in CF-based models, CF methods are challenging to implement on thin layers because there may not be sufficient data to extract a robust exponential curve, which may be noisy as a result. A general guideline may be to consider the use of CF only when the layers to be extracted comprise more than 15 pixels.

Table 1 Advantages, limitations, assumptions, and clinical applications of various implementations of AC measurement.

Methods	Advantages	Assumptions	Limitations	Demonstrated clinical applications
MS model (Almasian et al.,[17] Thrane et al.[18])	Considers multiple light scattering events, allowing more comprehensive analysis	Light scatters more than once.	Complicated computations.	Atherosclerotic plaque[20]
CF (Faber et al.[16])	Removes shadowing and other OCT imaging artifacts, which enables higher resolution	In-focus, SS Paraxial approximation; probe beam is not distorted by tissue	Requires averaging over a large amount of measured data points (50 to 100 A-scans); therefore, only relatively global AC measurements can be achieved	Atherosclerotic plaque;[2,21,28] prostate cancer[29]
3D CF (Gargesha et al.[22])	Applies noise reduction filtering and estimates AC from small volumes of interest (VOIs) rather than traditional A-line analysis	The VOI regions are relatively homogenous	Needs analysts to choose homogeneous VOIs for classification	Atherosclerosis[22]
CF with a reference layer (Vermeer et al.[27])	Improves lateral resolution and generates AC maps	An internal reference layer already exists in the tissue sample	Requires robust segmentation of the layers	Retinal imaging, early diagnosis of glaucoma[5]
DR (Vermeer et al.[15])	Allows pixel-wise estimation; works for multi-layered tissue	Light is attenuated completely; the backscattering and attenuation are linearly related	Focal plane must be placed high above the sample, making certain applications impractical; confocal function is assumed to be constant, which reduces SNR; noise at the pixel-level reduces accuracy	Cerebral ischemia monitoring;[7] atherosclerotic tissue;[4] choroidal thickness and vasculature assessment[30]
DR confocal (Smith et al.[23])	Fully automated pixelwise quantification of AC; can estimate AC when the focal plane is within the sample	Reflectivity is proportional to the full AC	Requires information on the confocal function parameters of the OCT system, such as focal plane depth and apparent Rayleigh range	
ODRE (Liu et al.[26])	Addresses one assumption of DR method: light is completely attenuated at the bottom	Attenuation is caused by scattering only; absorption is ignored.	Requires a rather thick bottom layer (approximately 120 pixels).	Cerebral ischemic stroke visualization[26]

The introduction of the DR algorithm was intended to improve the estimation accuracy by allowing pixelwise AC extraction.[15] Importantly, the DR method can easily be implemented on thin tissue layers. However, in the original method reported by Vermeer, the confocal point spread function is assumed to be a constant, so the focal plane is placed above the sample.[15] This situation is reasonable to create with a benchtop OCT system, and DR can be particularly useful in this case, even if the system parameters such as the confocal function cannot be characterized. Conversely, the assumptions of the DR model preclude certain clinical applications, where the focal plane may be placed in the sample (e.g., handheld systems with little control over the position of the system), and it also reduces the signal-to-noise ratio of the resulting measurements since the focal plane is typically the location of highest signal due to concentration of photons there. Successive studies in 2015 and 2019 were aimed to address these limitations.[14,23] The DRC method by Smith et al. considered the effect of the confocal PSF, which allows the focal plane to be placed within the sample and also included a more comprehensive sensitivity fall-off equation to further improve the signal-to-noise ratio.[23] However, in order to apply the confocal PSF, one needs to manually determine the system parameters, which makes clinical application more cumbersome. To fix this issue, Dwork et al. introduced an automated confocal parameter extraction algorithm that allows accurate pixelwise AC extraction without prior knowledge of OCT system parameters.[14] Dwork et al.'s work reduces the time needed for system calibration and therefore represents a step further toward clinical translation. Hence, the Dwork method for autoconfocal extraction allows the DR system to be used with *in vivo* clinical applications, such as endoscopy, although such demonstration has not yet been made. Recently, Liu et al. have developed ODRE method to address another assumption of Vermeer —that light is completely attenuated in the sample—and thus fixed the error with increasing imaging depth that can occur with the ordinary DR method.[26] ODRE allows accuracy extraction of AC from thinner tissues, accounting for the possibility of light being incompletely attenuated in tissue. In particular, this makes the ODRE method most suitable when it is anticipated or observed that the tissue is thick (or reasonably transparent), such that one does not expect all of the light to be absorbed by the bottom of the image range. In practice, the ODRE method still requires some prior knowledge of the tissue, because an exponential fitting step is performed at the end of imaging depth, which requires sufficient homogeneity in the bottom tissue layer. Hence, due to the hybrid nature of the ODRE algorithm, this method may still suffer from similar limitations of the CF methods if a suitable region for CF cannot be identified at the bottom of the image.

Table 1 presents an overview of the various methods for OCT-based AC extraction discussed above and provides an overview of clinical applications demonstrated with each method. The clinical application of AC is the subject of Sec. 3 of this review.

3 Clinical Applications

Because of its ability to provide quantitative tissue information with excellent resolution, AC measurement has been used in many clinical applications, including for ophthalmology, cancerous tissue detection, brain injury monitoring, and atherosclerotic plaque characterization. One of the earliest applications of AC measurement is in the characterization of atherosclerotic arteries,[3,20] where calcified, lipid-rich, and necrotic regions of a plaque were differentiated based on different AC values. Recently, AC has gained increasing popularity among other types of disease assessments; emerging AC applications include glaucoma detection,[5] reactive lymph nodes detection,[6] detection and grading of cancer,[7,8,31,32] and visualization and monitoring of brain injuries.[9,26,33,34] Given the quantitative and highly resolved tissue information that AC measurement provides, AC has presented itself as a promising analysis to be embraced by an even wider field of clinical studies.

3.1 *Ophthalmology*

3.1.1 *Glaucoma assessment*

van der Schoot et al.[5] and Vermeer et al.[27] applied measurement of the AC to differentiate glaucomatous tissue from normal retinal tissue, specifically in the RNFL. Traditional OCT has long been used to visualize morphological changes in the retina.[35] Because a decrease in the thickness of the RNFL has been associated with the presence of glaucoma, the signal intensities have been used to detect layer boundaries for determining the thickness of RNFL.[35] However, other than RNFL thickness measurement, previous studies have limited the application of OCT to mainly visualize morphological changes. Such qualitative information could suffer from variability due to different OCT systems and imaging artifacts; therefore, quantitative assessment of glaucoma with OCT is needed. Recent studies have shown that the reflectivity in the RNFL layer decreases in glaucomatous eye.[5,36] This diminished scattering effect can be quantified with the measurement of AC in the RNFL.

An elevation of intraocular pressure is normally seen in glaucoma patients, leading to the death of retinal ganglion cells.[36] The retinal ganglions cells are neurons of the central nervous system, whose cell bodies reside in the inner retina and whose axons form the optic nerve. Rapid degeneration of these cells results in damage of the optic nerve, which leads to irreversible vision loss. The decrease of reflectivity in the RNFL layer could be caused by the death of the ganglion cells,[36] resulting in a reduced density of nerve fibers in the RNFL and thus a reduced AC.

Vermeer et al. used CF, with the RPE serving as a reference layer,[27] to extract the AC values for healthy, mildly glaucomatous, moderately glaucomatous, and severely glaucomatous eyes (AC values of 4.78 ± 0.46 mm^{-1}, 4.09 ± 0.34 mm^{-1}, 3.14 ± 0.22 mm^{-1}, and 2.93 ± 0.33 mm^{-1}, respectively). The AC results show that the AC in the RNFL decreases as the level of glaucoma progresses. van der Schoot et al. hypothesize that the decrease in AC is related to pathological changes in the eye and is due to the reduction of nerve fiber density in glaucomatous RNFL that occurs when ganglion cells degenerate.[5,37] In previous studies, the decreased density has been associated with RNFL tissue property changes such as the reduction of birefringence and reflectance in the RNFL even prior to the thinning.[38–40] The hypothesis is that the decrease in ganglion cell axon density also leads to less scattering in the RNFL, which in turn causes diminished AC values. As the glaucoma stage advances, the axon density will continue to decrease, resulting in reduction of the AC. Therefore, AC can serve as an indicator of glaucoma presence and severity even prior to when structural changes can be visualized. Vermeer et al.[27] also generated en face AC maps, which allows visualization of attenuation patterns in the retina of both healthy and glaucomatous eyes along with corresponding thickness maps, as shown in Fig. 6. Vermeer

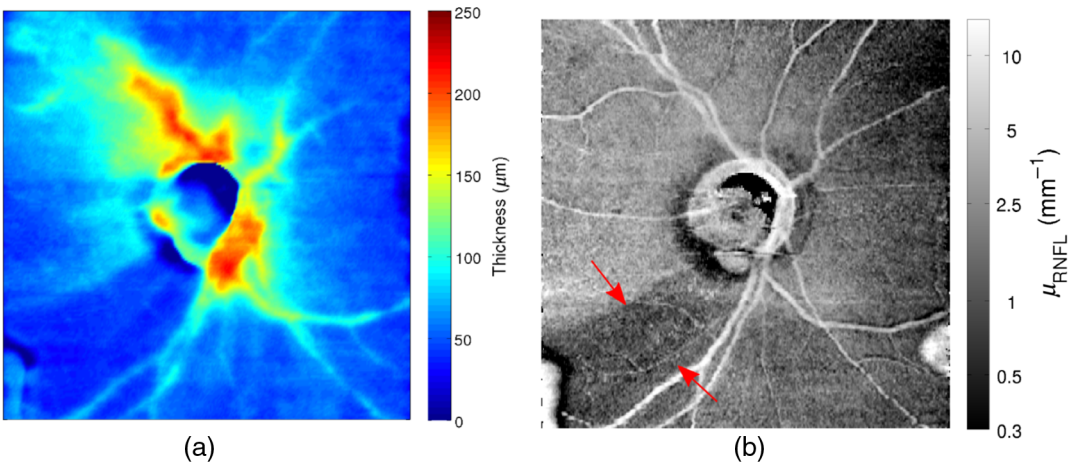

Fig. 6 (a) RNFL thickness mapping versus (b) RNFL AC plot of a glaucomatous eye. Red arrow indicates the location of affected tissue, which coinciding with reduced thickness in inferotemporal region (reprinted with permission from Ref. 24).

concluded that AC measurement provides comparable results to the thickness measurements and shows promising potential in early glaucoma assessment and diagnosis.

3.1.2 *Choroidal thickness and vasculature assessment*

Choroid plays an important role in maintaining normal functions of the eye, and, as a result, increasing attention has been focused to the study of choroidal thickness and vasculature in ocular diseases. To precisely measure the thickness of the choroid layer, successful segmentation of the choroid from sclera is important. However, due to the physiological location of choroid, light is mostly attenuated by the RPE before reaching choroidal structures, causing low contrast in these regions on OCT images. To address this issue, Zhou et al.[30] proposed an AC-based correction method to improve the contrast, which allowed successful segmentation of the choroid layer and imaging of choroidal vasculatures. In their approach, the DR method was used to obtain a pixelwise depth-reflectivity profile. With attenuation correction, the contrast at the choroid–sclera interface (CSI) is greatly improved, which allows successive segmentations steps, i.e., flattening at Bruch's membrane and graphic search for CSI, to carry out more reliably. The paper shows that with attenuation corrected segmentation, the algorithm is able to provide a more accurate choroidal thickness map with ultrawide field-of-view. Moreover, when AC correction is applied, the effect of shadows caused by large vessels in conventional B-scans can be reduced and thus eliminate imaging artifacts that may present in the appearance of an actual vessel. The paper reports excellent intravisit repeatability for both choroidal thickness maps and vasculature by calculating the coefficient of correlation (CV) for mean thickness (CV $= 1.7 \pm 0.7\%$) and vessel density (CV $= 0.41 \pm 0.18\%$).[30] However, a limitation of this method is that it can only correctly represent choroidal vessel patterns in healthy eyes with normal RPE, because the minimum intensity projection approach used to visualize choroidal vessel is based on the light scattering in RPE layer. In disease states, such as glaucoma, there is a notable reduce in some regions of the RPE layer, which may affect the accuracy in choroidal vasculature detection with the proposed method.

3.2 *Cancer Detection/Grading*

3.2.1 *Axillary lymph nodes detection for breast cancer patients*

The network of lymph nodes and vessels in the lymphatic system is a major vehicle by which cancer cells metastasize.[41] For example, axillary lymph nodes are examined in early-stage breast cancer patients to determine whether metastasis has already been taken place. The current gold standard examination of metastasis in lymph nodes is through histological assessment of excised lymph nodes.[42] In breast cancer patients, axillary clearance is normally performed to examine the presence of metastatic deposits in the nodes. However, this invasive procedure can lead to chronic issues such as lymphedema, which results from lymph fluid retention in the upper limbs.[43] Moreover, in many cases, uninvolved healthy lymph nodes are dissected, meaning that a significant number of unnecessary biopsies are performed. Therefore, to avoid excising healthy nodes, researchers have investigated alternative imaging modalities such as OCT.[44,45] Metastatic deposits in a lymph node can cause an increase in scattering as compared to surrounding normal tissue; the increased scattering results in a higher intensity in the observed OCT signals of the affected region.[45]

In order to further quantify this information, Scolaro et al.[6] used the SS model and applied the method of AC estimation to axillary lymph node assessment. Excised lymph nodes from patients were first imaged with OCT; after imaging, the tissue sections were prepared for histology. Their results showed that the resulting AC mapping provided greater contrast than the conventional OCT image, and the contrast was significant enough to improve identification of tissue features, such as vessels (V), medullary sinuses (MS), and lymphovascular spaces (LVS), as shown in Fig. 7. The identified regions also corresponded well with histological images. By extracting the AC in reactive nodes, necrotic regions (N) within the node could be determined, as they show higher attenuation ($\mu \approx 13$ mm^{-1}) compared to healthy nodes ($\mu = 4.5$ mm^{-1}). In dystrophic calcifications (C) within the necrotic tissue, the AC value is even higher: $\mu > 16$ mm^{-1}. The increase in AC value is due to the enlarged cells in metastatic deposits, which have a greater organelle intensity contributing to the scattering effect.

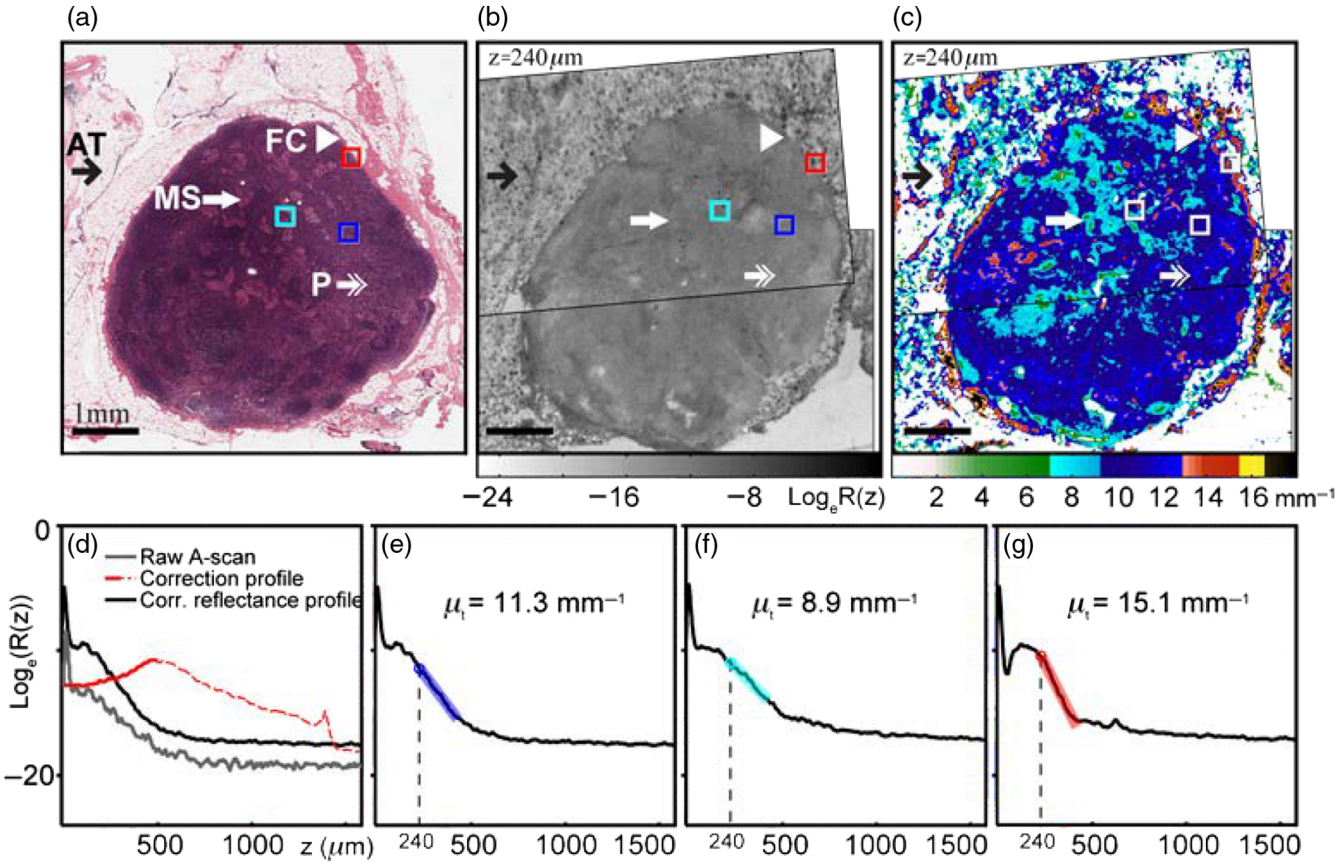

Fig. 7 (a) H&E stained histology, (b) en face OCT image, and (c) AC map of a healthy lymph node at a depth $z = 240$ μm. (d) Example of correction profile (red) used to correct the raw A-scans (gray) and generate the corrected reflectance profile (black). (e)–(g) Averaged A-scans of colored boxes are shown, where x axis is depth and by linear fitting identifiable features in lymph node can be identified: (e) paracortex (dark blue), (f) medullary sinuses (light blue), and (g) fibrous capsule (red) (reprinted with permission from Ref. 4).

However, the researchers also noted that AC measurement does not identify all tissue features equally well: in one of the samples, the thickened reactive fibrous capsule has an AC estimation of $\mu = 11.8 \pm 0.2$ mm^{-1}, which was very similar to the AC value of the paracortex: $\mu = 10.4 \pm 0.4$ mm^{-1}. Overall, the researchers concluded that the method of AC estimation improved characterization and differentiation between healthy and metastatic axillary lymph node tissue.

3.2.2 *Bladder cancer detection*

Cauberg et al. applied AC measurement to the assessment of bladder urothelial carcinoma (UC), with the aim of achieving real-time grading of UC. Grading of UC is determined based on morphological changes of the urothelium, and this parameter is important in clinical management of patients, who experience small recurrent bladder tumors.[7] Currently, the clinical approach for grading is histopathology, which does not provide real-time information regarding disease progression and is limited to only certain clinical scenarios (i.e., harvesting tissue is required).[46] To avoid unnecessary biopsies and improve accuracy of the grading process, real-time qualitative assessment of the bladder tissue is desired.

Given previous demonstrations that tissue scattering properties vary with stage (hyperplasia, dysplasia, and neoplasia) in rat models of bladder cancer[47] and results from other studies showing that the AC can differentiate morphological changes in cases of atherosclerotic plaques and necrotic human fibroblasts,[2,3,48] Cauberg et al. hypothesized that measurement of AC could serve as a real-time indicator for UC grading. The biological basis of this hypothesis is that as UC grade increases, mitotic activity in the urothelium increases, the cytonuclear ratio changes, and polarity of the urothelium decreases.[7] The AC of bladder tissue was extracted from OCT data using the CF method and tested on *ex vivo* tissue samples from patients with single or multiple bladder tumors, positive cytology, and negative cystoscopy (suspicious lesions). The standard reference diagnoses were made by three independent pathologists, who classified each of the histological slides into four categories: normal, UC grade 1, UC grade 2, and UC grade 3. Then, a consensus diagnosis was made by all three pathologists for each histology to address the high subjectivity and interobserver variability typically present in histopathological grading. Based on the grading information, the median AC of each category was reported to be 5.75, 5.52, 4.85, and 5.62 mm^{-1} for normal tissue, and UC grades 1, 2, and 3 respectively.[7] The measured AC values did not validate the hypothesis, as it was not possible to differentiate tissues of different categories. The researchers reasoned that the lack of correlation between AC and UC grade could be due to the subjectivity in the reference standard (histological grading), the small sample size, or most importantly, the *ex vivo* nature of this study.[7] Because of the heterogeneity of

bladder tumors, multiple grades could exist in one tumor,[32,49] which complicates the grading process. Another possible reason that might account for the lack of correlation was the discrepancy between the OCT image site and the actual histology slide.[7] Also, there was a discrepancy in the way that grading was determined: by the presence of one or two morphological changes for the histological slide, compared to use of CF for the AC estimation approach, which averaged tissue information across the entire slide. Therefore, one possible improvement of their experimental setup is to try the DR AC estimation, which would allow pixelwise, local determination of tissue properties.

3.2.3 In vivo *staging and grading of urothelial carcinoma*

Traditionally, biopsies have been used for staging and grading of upper urinary tract urothelial carcinoma (UTUC). However, there has been an increasing number of nondiagnostic biopsies and inaccurate diagnosis, resulting in up-staging and grading of UTUC. This inaccuracy is due to the anatomical limitation of the upper urinary tract, which results in smaller and crushed biopsy samples. Accurate staging and grading are important to patient enrollment of curative surgery, as only patients with advanced grade lesions will be selected for ureterectomy, whereas others may be applicable for conservative treatments.[50] To seek additional diagnostic information, in 2016, Bus et al. applied AC measurements from OCT to *in vivo* staging and grading of upper tract UC. The AC results for lesion staging showed high agreement (87%) with histopathology and also high sensitivity (100%) and specificity (92%). They also showed that there are significant differences in the AC of low-grade lesions and that of high-grade lesions (measured median equals 2.1 and 3.0 mm^{-1}, respectively), suggesting that AC measurements can be used for lesion grading. When using a cutoff AC of 2.4 mm^{-1}, the resulting sensitivity and specificity are 87% and 90%, respectively. This cutoff value was further investigated by Freund et al. in 2019, where OCT imaging data from 35 patients with papillary UTUC were used in the study (data taken from the 42 patients imaged by Bus et al.) and yielded a cutoff value of 4.0 mm^{-1} with a sensitivity of 83% and a specificity of 94% for high-grade papillary UTUC.[51] Freund et al. improved Bus's algorithm by calibrating the confocal function parameters and sensitivity roll-off individually, whereas in the previous experiment, Bus et al. assumed that the focus was at the tissue boundary and the effects of the confocal point spread function and roll-off were approximated as a single offset.

The AC estimation method Bus and Freund used follows Faber et al.'s CF approach[16] and, therefore, has the limitation of not being able to include thin layers for grading due to the lack of sample points and urothelium thickness needed for AC extraction. One possible improvement can be made by employing Vermeer's DR method, which can perform AC extraction on superficial or thin tissue layers. Reported false positives in this study are caused by large tumors and inflammation. This is due to the limited light penetration depth of OCT systems, as the layered structures in tumors exceeding 2 mm in thickness cannot be effectively visualized with OCT, leading to inaccurate staging. Nevertheless, Bus et al. and Freund et al. have shown that AC measurements can provide comparable if not better diagnostic accuracy of UTUC compared to biopsy, and AC analysis has the potential for real-time grading and staging during ureterorendoscopy.

3.2.4 *Cancerous colon tissue detection*

Zhao et al.[8] applied the AC measurement to early detection of adenomatous colon tissues. The current gold standard detection method of colon cancer is via colonoscopy;[52] however, this method only allows visualization of superficial changes in tissue morphology, so precancerous changes in deeper layers cannot be detected. In colon adenocarcinoma, morphological changes occur in malignant tissues, including increasing microvascularization, distortion of the collagen matrix, and increasing blood and protein concentration.[53] These changes result in variations of the permeability of analytes, such as glucose, across colon tissue, and this variation can be measured by monitoring the analyte diffusion rate in normal and cancerous tissue.[54] Zhao's group studied the diffusion rate of glucose in colon tissue by measuring both the OCT signal slope (OCTSS) and extracting AC from the OCT data.[8]

The author analyzed the changes in OCTSS and AC values of both normal and adenomatous *ex vivo* colon tissues with topical application of 30% glucose solution and made several observations.[8] Without glucose application, the backscattering OCT intensity is greater in cancerous tissues compared to normal tissues. This difference is due to the enlarged nuclei in tumor cells and the overall higher density of tumor cells in adenomatous tissue.[55] With glucose applied to tissues, the adenomatous tissue showed a steeper decrease of OCTSS than normal tissue, meaning that there was greater reduction in scattering inside cancerous colon tissue due to more glucose uptake. Therefore, glucose is more permeable in cancerous tissue than normal tissue (with a permeability coefficient $= 5.65 \pm 0.24 \times 10^{-6}$ cm s^{-1} and $3.37 \pm 0.17 \times 10^{-6}$ cm s^{-1} for adenomatous and normal tissue, respectively). In agreement with the observation of permeability change, the measured AC values also decreased with time after administration of glucose solution, as glucose slowly diffused into tissue; in adenomatous tissues, the ACs experienced a much more rapid decrease. Furthermore, the AC values of cancerous tissue are significantly higher than normal colon tissue, with a maximum AC of 8.48 ± 0.95 mm^{-1} versus 3.48 ± 0.37 mm^{-1} and a minimum of 3.16 ± 0.69 mm^{-1} versus 2.68 ± 0.82 mm^{-1}, in cancerous tissue and normal tissue, respectively. The author concluded that this notable increase in the AC was due to the increase in microvascularization in adenomatous colon, which resulted in a higher concentration of hemoglobin and fibrin in the affected region as compared to its surrounding, leading to a higher scattering in cancerous tissue.[20] In conclusion, the measurement of AC in colon tissue is able to identify colon adenocarcinoma *ex vivo*, which may be useful in early detection of colon cancer *in vivo*.

3.2.5 *Differentiation between renal cell carcinoma vs oncocytoma*

Small renal masses (SRM), which are renal masses with a diameter less than 4 cm, have shown a steady increase in clinical incidence and are responsible for 68% of renal cell carcinomas (RCC).[56] While abdominal imaging modalities such as CT and MRI are effective in detecting SRMs, it is difficult to differentiate between benign oncocytoma and malignant RCC tumors, which may lead to overtreatment of benign SRMs when it is not necessary. Other clinical solutions that have been used to assess SRMs include biopsies; however, for SRMs, the rate of nondiagnostic biopsies is as high as 30%, which results in time-consuming repeats.[57]

Wagstaff et al.[56] addressed this issue by applying percutaneous needle-based OCT and the resulting AC to the differentiation between oncocytoma and RCC and among three subtypes of RCC: clear cell renal cell carcinoma (ccRCC), papillary renal cell carcinoma (pRCC), and chromophobe renal cell carcinoma (chRCC). Their results showed that the median AC value of oncocytoma (3.38 mm^{-1}) was significantly lower than the median AC of RCC (4.37 mm^{-1}). From the results of their ROC curve, the cutoff value for malignant tumors was determined to be 3.85 mm^{-1}, which yielded a sensitivity of 86% and specificity of 75%. Also, the results have shown that there are significant differences between the AC values of oncocytoma versus ccRCC, and of oncocytoma versus pRCC (3.38 versus 4.36 mm^{-1}, and 3.38 versus 4.79 mm^{-1}, respectively), whereas there is no significant difference between AC of oncocytoma vs chRCC (3.38 versus 3.58 mm^{-1}). Limitations to Wagstaff's study include that the use of OCT probe delivery is restricted by the tumor location. Hence, anterior SRMs and tumors located near the diaphragm might be excluded from this presented method, due to the risk of internal damage of proximate organs.[56]

3.2.6 *Ovarian tissue compares collagen content in malignant and normal tissue*

Yang et al. extracted optical AC from healthy and malignant ovarian tissues and found a correlation between the collagen content of tissue and its attenuation due to scattering.[31] Yang et al. applied the SS model for analysis of the OCT signals and assumed that the attenuation of light in ovarian tissue was mainly caused by scattering. The biological basis of their approach is that malignancy in ovarian tissues can reduce collagen content, which is the main scatterer in ovarian tissue and change the directivity of ovarian stroma, which is composed of collagen fibers.[58] The reported scattering coefficients in healthy and malignant ovarian samples were 2.41 mm^{-1} ($\pm$0.50) and 1.55 mm^{-1} ($\pm$0.46), respectively. After imaging, the tissue samples were sectioned and stained with Sirius Red (SR). The collagen content was measured as the collagen area fraction (CAF), which equals the ratio of the SR-stained collagen area over the total histological tissue area. The CAF obtained at the OCT imaging plane from normal samples was 48.4% ($\pm$12.3%) and that from the malignant samples was 11.4% ($\pm$4.7%).[31] The results of CAF and scattering coefficients in normal and malignant ovarian tissue samples show that the AC can be used for characterization of neoplastic changes in the ovary and has the potential of detecting ovarian cancers.

3.2.7 *Prostate cancer detection*

A minimally invasive, needle-based OCT system was developed by Muller et al. and qualitative AC analysis was performed to differentiate among benign stromal tissue, inflammation, and different grades of prostate cancer (Gleason scores 3 and 4).[29] In this study, one-to-one registration of OCT en face AC mapping and histology slide was achieved to ensure accurate classification.[59] CF method was used to extract AC measurements for specific regions of interest. Study results showed that while malignancy, inflammation and benign tissues could be identified, the tissues exhibited similar patterns, which contribute to challenge in differentiation. AC analysis was helpful in quantitatively categorizing tissue types and results in significant median AC values among benign and inflamed stroma, and Gleason 3 and Gleason 4 malignancy (4.6, 4.1, 5.9, and 5.0 mm^{-1}, respectively).[29] However, the authors did report differences in AC measurements within individual patients. For example, the AC measurements of Gleason 4 region in one patient could differ up to 2 mm^{-1}. The authors reasoned that this variation could be due to the heterogeneity of the malignant region and thus increased classification challenges for the pathologist. Also, more heterogeneous tissues such as cysts were not studied due to the same reason despite its clinical significance. The author suggested that pattern recognition algorithm or convolutional neural networks could be useful in differentiation prostate cancers with OCT.

3.2.8 *Brain cancer detection*

Complete detection and removal of brain cancer is crucial to patients' survival; however, it is often challenging because infiltrative regions of cancer are difficult to distinguish from healthy tissues.[60] Therefore, there is a need for accurate, intraoperative visualization of cancerous regions in the brain. AC studies have been conducted on *ex vivo* mouse brains[61] and *ex vivo* human brains for brain cancer detection,[62,63] as well as *in vivo* mouse models to demonstrate the feasibility of intraoperative visualization of cancerous tissue with AC mapping.[62] In 2015, Kut et al.[62] extracted AC from various regions (cancer core, infiltrative zone, and surrounding noncancerous tissue) of low-grade and high-grade cancer tissues of *ex vivo* human brains. The reported AC values from high-grade cancer tissues are 3.9, 3.5, and 6.2 mm^{-1}, for cancer core, infiltrated zone, and noncancer tissue, respectively. In low-grade cancer tissue, the corresponding values are 4.0, 2.7, and 6.2 mm^{-1}. The results show that the noncancer regions have AC measurements that are significantly higher than both infiltrated zones and cancer cores; however, there is no significant difference for high- versus low-grade cancers in both the infiltrated zone and cancer core. In a more recent study by the same group,[63] the AC extraction algorithm was improved to ensure accurate AC estimation in the face of incorrect tissue surface detection, which further increases the potential of AC for *in vivo* clinical translation.

3.3 *Brain Injury Visualization*

OCT has been applied to imaging physiological changes in the brain in response to traumatic brain injuries (TBI) such as stroke. Microvascular changes,[11] cerebral ischemia,[9,26,33,64] and cerebral edema[34] have been visualized and analyzed with the optical AC.

3.3.1 *Cerebral ischemic stroke*

Cerebral ischemia following stroke is a serious medical condition in which the affected site experiences drastically reduced blood perfusion, creating a hypoxic environment. Due to hypoxia, ischemic stroke causes depletion of oxygen and nutrients in the neurons, leading to severe brain tissue damage.[65] Affected tissues will experience loss of function and altered cellular structures, and this change in tissue properties can result in altered light attenuation in affected regions.[33]

Srinivasan et al.[64] applied analysis of the optical AC to ischemic stroke and reported that the intrinsic scattering properties of cerebral tissue can indicate acute cellular and vascular injury and recovery events during strokes. They found that the scatter characteristics were different in ischemic tissues and intact tissues by plotting the logarithmic OCT signal versus imaging depth in the

brain. They also observed reduced light penetration in infarcted regions and concluded that there is an increase in the scattering property of affected cells. Their explanation of the increased scattering was because of the swelling of cells and intracellular organelles upon cerebral ischemia.[64]

Baran et al.[9,11] introduced OCT-based tissue injury mapping (TIM), where they combined Vermeer's DR extraction of optical AC with optical microangiography (OMAG),[15] and demonstrated its ability to depict changes in tissue properties by characterizing light attenuation in tissue. TIM uses the sorted average intensity projection (sAIP) algorithm, which sorts the extracted optical attenuation values of each A-line in an ascending order. Then, the sorted ACs are averaged using the following equation:

$$\mathrm{OAC}_{\mathrm{average}}[y] = \frac{\sum_{i=(N/2)-(M/2)}^{(N/2)+(M/2)} \mathrm{OAC}_{\mathrm{sorted}}[i]}{M}, \tag{25}$$

where N is the total number of pixels in a selected portion of an A-line and M is an adjustable parameter representing the number of pixels to be averaged. After sAIP and averaging, fluctuations in the AC values can be removed, and thus, smooth en face AC mappings can be produced. In their study, a mouse model of middle cerebral artery (MCA) occlusion was used and images were taken prior to 1 day and 3 days after the occlusion. The result shows that the average AC value in ischemic regions (MCA) increased by 70% as compared to the baseline, and the value continued to increase by another 20% of 3 days after occlusion. The difference between ischemic and unaffected regions [perfused by the anterior cerebral artery (ACA)] in AC mapping agrees with the findings from OMAG mapping, where both vessel dilation and increased vessel density were found postocclusion. However, en face optical attenuation coefficient (OAC) mapping provides a clearer distinction of the ischemic (MCA) regions from the ACA regions. Both Srinivasan's and Baran's work provide qualitative information regarding changes in the cerebral tissue following cerebral ischemia and demonstrate the effectiveness of AC in depicting tissue changes.

Recently, Liu et al. developed ODRE and provides quantitative AC values in both ischemic and intact cerebral tissues of mouse models of focal ischemia.[26] They found the same increasing trend in ischemic cerebral regions as the previous papers and showed that the AC increased by 1 mm^{-1} within 120 min following MCA occlusion, as shown in Fig. 8. Choi et al. also applied AC analysis in their multiparametric OCT imaging of a mouse model of permanent focal ischemia, where they found an increase in AC of the cortical regions around focal ischemia (>3 mm^{-1}) as compared to that of undamaged grey matter (1.01 mm^{-1}). Choi et al. also noticed that the ischemic effect expanded over time and the rim of the cortical area developed an even greater AC (>4.5 mm^{-1}) 8 min postocclusion.[33]

3.3.2 *Cerebral edema*

Cerebral edema is a condition in which excess water accumulates in the brain after TBI, increasing intracranial pressure (ICP) and leading to many secondary injuries due to the mechanical compression to adjacent brain structures.[66] Current assessments of cerebral edema include ICP monitoring and brain water content (BWC) analysis. However, ICP only provides a global measurement of the pressure and cannot be used to assess brain edema in local regions; BWC analysis may require biopsies and thus, the procedure can be invasive.[34] Therefore, a real-time *in vivo* imaging method that could accomplish both temporal and spatial assessment of cerebral edema would be highly beneficial. Rodriguez et al.[34] imaged the cerebral cortex with OCT and found that the optical scattering property of the cerebral tissue was changed as edema progressed, causing the average AC in the cerebral cortex to decrease.

In their experiment, an acute water intoxication model of cytotoxic cerebral edema was used, resulting in increasing water content in the brain due to the osmotic gradient. After intraperitoneal (IP) injection of water into an experimental mouse group, the mouse brain was imaged with a spectral-domain OCT system (centered at 1300 nm). After data collection, the mice were euthanized and their brains dissected for BWC, the gold standard for brain edema. Results showed that there was a linear decrease in the AC value after water injection and reached a maximum decrease of 8%. The BWC results confirmed that the experiment group had greater water content in the brain than the control (no IP injection).

3.4 *Atherosclerosis Plaque Characterization*

Thin-cap fibroatheroma (TCFA) rupture is a major cause of acute myocardial infarctions.[3] Therefore, successful identification and visualization of TCFA can help with our understanding

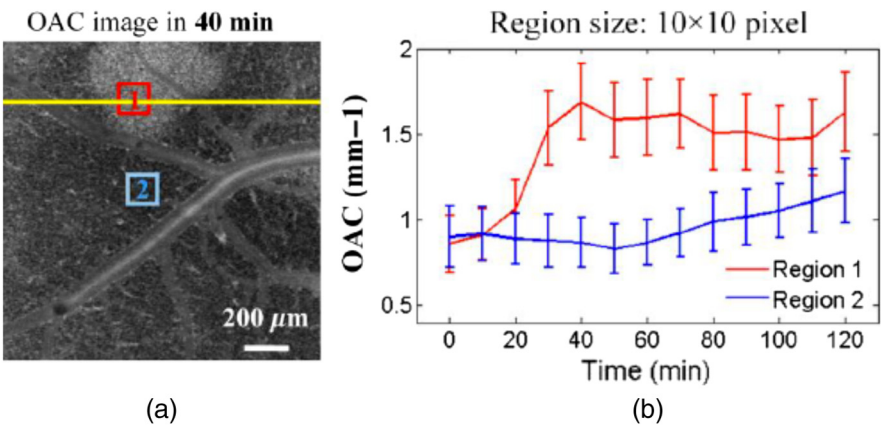

Fig. 8 (a) and (b) Changes in two regions of brain tissue OAC as a function of time. Region 1 (red box area): ischemic damaged regions; region 2 (blue box area): undamaged regions (reprinted with permission from Ref. 26).

and treatment strategies of this type of rupture-prone plaques. Important parameters that aid the determination of plaque vulnerability include the thickness of fibrous cap, degree of inflammation, intraplaque hemorrhage, and plaque tissue composition.[22] Conventional OCT imaging has been used to determine the vulnerability of plaques due to its high resolution, as it provides detailed structural information regarding vessel wall and plaque tissues;[22] however, the border between different types of tissues (i.e., fibrous and lipid-rich) can sometimes be ambiguous. Levitz et al.[20] first applied AC analysis to the differentiation of *ex vivo* normal and atherosclerotic arterial tissues and demonstrated that AC can distinguish dissimilar tissue type based on the optical properties of tissues. The AC extraction method employed is based on the MS model developed by Thrane et al.[18] Levitz's study showed a difference in the scattering properties of healthy and atherosclerotic tissues; 95% of normal arterial wall tissues had AC values between 15 and 39 mm^{-1} and approximately 60% of lipid-rich and fibrocalcific plaques have AC values lower than 15 mm^{-1}.

In 2005, van der Meer et al.[2,28] applied AC measurement for characterization of arterial wall and atherosclerotic plaque components, using CF (based on the SS model) on averaged OCT A-scans.[2,28] They concluded that the AC is highest in the calcification region and thrombus (11.1 ± 4.9 mm^{-1} and 11.2 ± 2.3 mm^{-1}, respectively), intermediate in the intimal and media layers (5.5 ± 1.2 mm^{-1} and 9.9 ± 1.8 mm^{-1}), and lowest in lipid-rich regions (3.2 ± 1.1 mm^{-1}).

In 2008, Xu et al. also applied CF to characterization of atherosclerotic plaques in human coronary arteries.[3] Different from the previous studies that have used the scattering coefficient as the quantitative tissue parameter,[18,49,50] Xu et al. measured both the total AC μ_t and the backscattering coefficient μ_b in order to avoid overlaps of parameter measurements between tissue types and ensure significant separation. Moreover, alternative to that taking measurements from longitudinal cut of the artery (imaging from the lumen side), this group sectioned the artery in the transverse plane. The three major features Xu et al. aimed to identify were fibrous tissues, calcified tissues, and lipid-rich tissues. Their reported μ_t and μ_b values are 5.7 ± 1.4 mm^{-1} and 4.9 ± 1.5 mm^{-1} for calcified plaques, 6.4 ± 1.2 mm^{-1} and 18.6 ± 6.4 mm^{-1} for fibrous plaques, and 13.7 ± 4.5 mm^{-1} and 28.1 ± 8.9 mm^{-1} for lipid-rich plaques. By creating a colormap of AC and backscattering coefficient, Xu et al. were able to more directly visualize plaque components, as shown in Fig. 9.

Further investigations were made by van Soest et al. in 2010 and Gargesha et al. in 2015, and both groups were able to determine AC values *in vivo* with a catheter-based approach.[21,22] Van Soest et al. found that lipid plaques had high AC ($\mu_t > 10$ mm^{-1}), whereas fibrotic and calcific plaques had lower AC (2 $mm^{-1} < \mu_t < 5$ mm^{-1}), which agreed with the μ_t measurements obtained by Xu. Gargesha et al. used a three-dimensional approach and estimated AC from small volumes of interest in order to avoid noise associated with a single A-line. The AC values from Gargesha's results are reported as 3.84 ± 0.95 mm^{-1} for calcified plaques, 2.15 ± 1.08 mm^{-1} for fibrotic plaques, and 9.99 ± 2.37 mm^{-1} for lipid-rich plaques, which have a similar general trend as the results of Xu and van Soest.

In 2017, instead of the CF technique, Liu et al. applied DR estimation in characterization of atherosclerotic tissues.[4] In their study, the DR method was further extended to extract the backscatter-related term from OCT images, which served as a complementary parameter to AC analysis. Liu's study achieved successful differentiation of six atherosclerotic tissue types, including mixed calcified plaque (1.68 ± 0.14 mm^{-1}), calcification (0.87 ± 0.24 mm^{-1}), fibrous (1.75 ± 0.48 mm^{-1}), lipid-rich (2.60 ± 0.13 mm^{-1}), macrophage (3.41 ± 0.38 mm^{-1}),

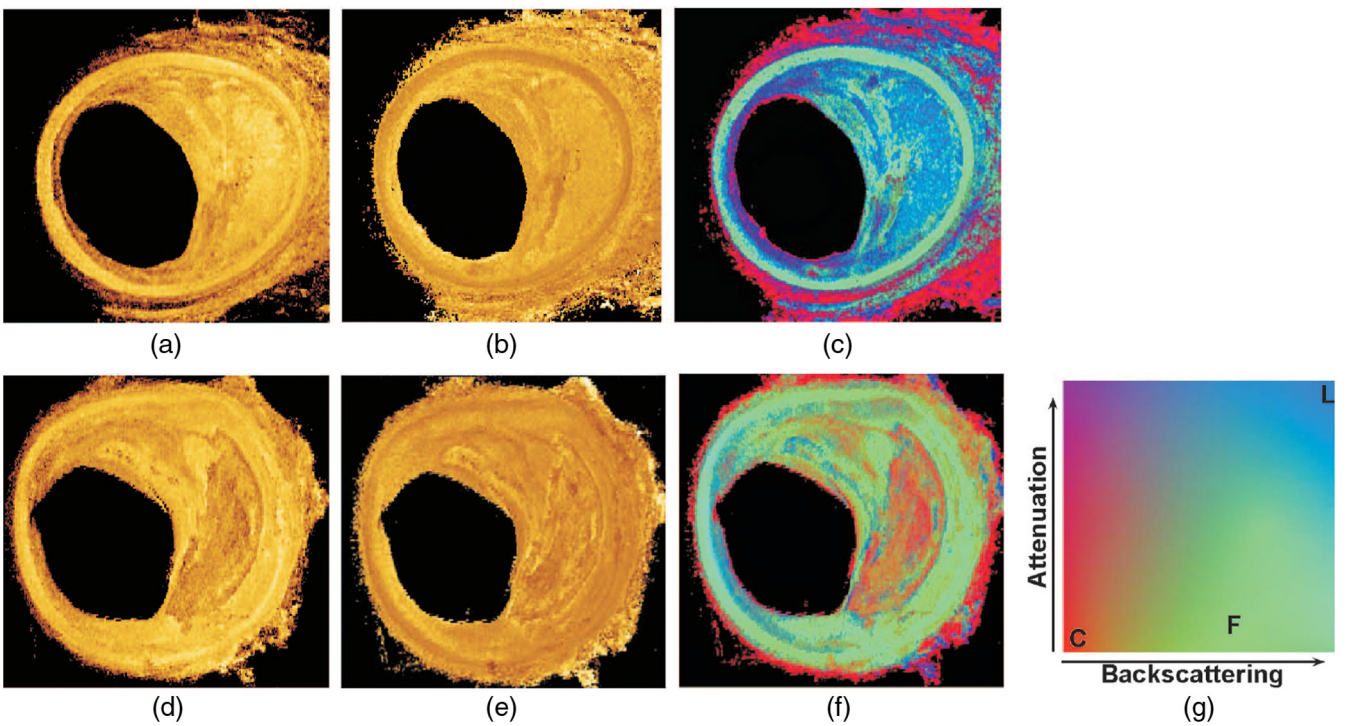

Fig. 9 (a, d) Backscattering and (b, e) attenuation coefficient images of artery segments with (g) color map combining (c, f) attenuation and backscattering coefficients. Upper row: lipid-rich plaque; lower row: fibrocalcific plaque (reprinted with permission from Ref. 3).

and necrotic core (1.89 ± 0.54 mm^{-1}) regions. From Liu's result, the comparative relationships between different tissues agree with the previous findings of Xu et al. and van Soest et al., i.e., calcified region has a lower AC than fibrous tissue.[3,21]

4 Future Directions

With the ability to quantitatively differentiate dissimilar tissues, AC has gained popularity in a number of clinical applications. The extraction technique can be further improved, however. While multiple efforts have already been made to improve the extraction accuracy of AC measurements, future investigations are needed to further improve performance of the algorithms and expand the range of clinical applications. Currently, there has been no study on three-dimensional automated AC extraction; such a study would be particularly useful for endoscopic clinical applications. Given the increasing popularity of the DR method, other possible improvements in AC estimation may be considered addressing the other assumption made in DR method[15] that the amount of backscattered light to the total scattered light is a fixed ratio. Almasian et al.[67] have demonstrated that the scattering coefficient is related to particle size and orientation. Current AC extraction methods have yet to account for such effects when the particle sizes and size distributions are unknown. Therefore, there is still the need to incorporate more detailed models for AC extraction so that AC tissue analysis can become more accurate in clinical contexts.

In order to further broaden the clinical applications of AC, spectroscopic AC may be introduced to improve the specificity. SOCT is a functional extension of OCT that combines light scattering spectroscopy with OCT.[68,69] This combination provides both spectroscopic and depth information, and by applying AC to wavelength-dependent scattering, one may conceive of a spectroscopic AC that may be capable of distinguishing even finer cellular structures. Spectroscopic AC may also help to avoid a potential danger of confusing a high-scattering low-absorption region with low-scattering high-absorption region across different tissues types, given the highly varying ratio of scattering and absorption coefficients in biological tissues.[70,71] For example, in a single-tissue section, areas containing blood vessels would have an AC value with much greater absorption coefficient contribution since blood is highly absorbing. However, in the context of the same tissue type with different pathological conditions, changes in AC can still adequately provide diagnostically meaningful information for detecting disease manifestation, as shown in most of the clinical application studies included in the review.

The lack of molecular specificity of OCT can also be addressed with multimodal systems, such as a combined Raman spectroscopy (RS) and OCT system, where the biochemical information provided by RS can help with distinguishing finer tissue structures.[72]

5 Conclusion

Optical AC, an underlying tissue property, is an important parameter that has been recently proposed to address the long-standing criticism of OCT, i.e., providing only morphological information. The analysis of AC enables quantitative assessment of tissue properties, facilitates tissue differentiations, and is relevant to many clinical applications. Extraction of this parameter is achieved through postprocessing of OCT interferograms. Ever since the first demonstration of AC extraction, many innovative methods have been introduced, and as a result, the measurement errors have been effectively reduced. However, more efforts need to be made for further improvement of extraction algorithms to address the assumptions made in current methods. The quantitative tissue properties from AC assessment have been shown useful in a wide range of clinical applications, currently in areas such as characterization of atherosclerotic plaques, monitoring of blood perfusion in ischemic stroke, and differentiation of cancerous tissues. As AC presents itself as a promising technique, we expect that it will continue to enhance the clinical impact of OCT and facilitate many more therapeutic and pathological investigations.

Disclosures

The authors acknowledge that there are no conflicts of interest.

Acknowledgments

We wish to acknowledge Francis Tsow and Behnam Tayebi for their help in preparing the manuscript. S.C. was supported by the Constantine A. Paras Memorial Fellowship.

References

1. D. Huang et al., "Optical coherence tomography," *Science* **254**(5035), 1178–1181 (1991).
2. F. J. van der Meer et al., "Quantitative optical coherence tomography of arterial wall components," *Lasers Med. Sci.* **20**(1), 45–51 (2005).
3. C. Xu et al., "Characterization of atherosclerosis plaques by measuring both backscattering and attenuation coefficients in optical coherence tomography," *J. Biomed. Opt.* **13**(3), 034003 (2008).
4. S. Liu, "Tissue characterization with depth-resolved attenuation coefficient and backscatter term in intravascular optical coherence tomography images," *J. Biomed. Opt.* **22**(9), 096004 (2017).
5. J. van der Schoot et al., "The effect of glaucoma on the optical attenuation coefficient of the retinal nerve fiber layer in spectral domain optical coherence tomography images," *Invest. Ophthalmol. Visual Sci.* **53**(4), 2424–2430 (2012).
6. L. Scolaro et al., "Parametric imaging of the local attenuation coefficient in human axillary lymph nodes assessed using optical coherence tomography," *Biomed. Opt. Express* **3**(2), 366–379 (2012).
7. E. C. C. Cauberg et al., "Quantitative measurement of attenuation coefficients of bladder biopsies using optical coherence tomography for grading urothelial carcinoma of the bladder," *J. Biomed. Opt.* **15**(6), 066013 (2010).
8. Q. Zhao et al., "*Ex vivo* determination of glucose permeability and optical attenuation coefficient in normal and adenomatous human colon tissues using spectral domain optical coherence tomography," *J. Biomed. Opt.* **17**(10), 1050041 (2012).
9. U. Baran et al., "Automated segmentation and enhancement of optical coherence tomography-acquired images of rodent brain," *J. Neurosci. Methods* **270**, 132–137 (2016).
10. P. Gong, "Assessment of human burn scars with optical coherence tomography by imaging the attenuation coefficient of tissue after vascular masking," *J. Biomed. Opt.* **19**(2), 021111 (2013).
11. U. Baran et al., "*In vivo* tissue injury mapping using optical coherence tomography based methods," *Appl. Opt.* **54**(21), 6448–6453 (2015).
12. D. M. Viviane et al., "Noninvasive monitoring of photodynamic therapy on skin neoplastic lesions using the optical attenuation coefficient measured by optical coherence tomography," *J. Biomed. Opt.* **20**(5), 051007 (2015).
13. M. Wojtkowski et al., "In vivo human retinal imaging by Fourier domain optical coherence tomography," *J. Biomed. Opt.* **7**(3), 457–464 (2002).
14. N. Dwork et al., "Automatically determining the confocal parameters from OCT B-scans for quantification of the attenuation coefficients," *IEEE Trans. Med. Imaging* **38**(1), 261–268 (2019).
15. K. A. Vermeer et al., "Depth-resolved model-based reconstruction of attenuation coefficients in optical coherence tomography," *Biomed. Opt. Express* **5**(1), 322–337 (2014).

16. D. J. Faber et al., "Quantitative measurement of attenuation coefficients of weakly scattering media using optical coherence tomography," *Opt. Express* **12**(19), 4353–4365 (2004).
17. M. Almasian et al., "Validation of quantitative attenuation and backscattering coefficient measurements by optical coherence tomography in the concentration-dependent and multiple scattering regime," *J. Biomed. Opt.* **20**(12), 121314 (2015).
18. L. Thrane, H. T. Yura, and P. E. Andersen, "Analysis of optical coherence tomography systems based on the extended Huygens-Fresnel principle," *J. Opt. Soc. Am. A* **17**(3), 484–490 (2000).
19. A. Knu, S. Bonev, and W. Knaak, "New method for evaluation of *in vivo* scattering and refractive index properties obtained with optical coherence tomography," *J. Biomed. Opt.* **9**(2), 265–273 (2004).
20. D. Levitz et al., "Determination of optical scattering properties of highly-scattering media in optical coherence tomography images," *Opt. Express* **12**(2), 249–259 (2004).
21. G. van Soest et al., "Atherosclerotic tissue characterization *in vivo* by optical coherence tomography attenuation imaging," *J. Biomed. Opt.* **15**(1), 011105 (2010).
22. M. Gargesha et al., "Parameter estimation of atherosclerotic tissue optical properties from three-dimensional intravascular optical coherence tomography," *J. Med. Imaging* **2**(1), 016001 (2015).
23. G. T. Smith et al., "Automated, depth resolved estimation of attenuation coefficient from optical coherence tomography data," *IEEE Trans. Med. Imaging* **34**(12), 2592–2602 (2015).
24. K. A. Vermeer et al., "Quantitative RNFL attenuation coefficient measurements by RPE-normalized OCT data," *Proc. SPIE* **8209**, 82090U (2012).
25. B. S. H. Yun et al., "High-speed spectral-domain optical coherence tomography at 1.3 um wavelength," *Opt. Express* **11**(26), 3598–3604 (2003).
26. J. Liu et al., "Optimized depth-resolved estimation to measure optical attenuation coefficients from optical coherence tomography and its application in cerebral damage determination," *J. Biomed. Opt.* **24**(3), 035002 (2019).
27. K. A. Vermeer et al., "RPE-normalized RNFL attenuation coefficient maps derived from volumetric OCT imaging for glaucoma assessment," *Invest. Ophthalmol. Visual Sci.* **53**(10), 6102–6108 (2012).
28. F. J. van der Meer et al., "Localized measurement of optical attenuation coefficients of atherosclerotic plaque constituents by quantitative optical coherence tomography," *IEEE Trans. Med. Imaging* **24**(10), 1369–1376 (2005).
29. B. G. Muller et al., "Needle-based optical coherence tomography for the detection of prostate cancer: a visual and quantitative analysis in 20 patients," *J. Biomed. Opt.* **23**(8), 086001 (2018).
30. H. Zhou et al., "Attenuation correction assisted automatic segmentation for assessing choroidal thickness and vasculature with swept-source OCT," *Biomed. Opt. Express* **9**(12), 6067–6080 (2018).
31. Y. Yang et al., "Optical scattering coefficient estimated by optical coherence tomography correlates with collagen content in ovarian tissue," *J. Biomed. Opt.* **16**(9), 090504 (2011).
32. L. Cheng et al., "Cancer heterogeneity and its biologic implications in the grading of urothelial carcinoma," *Cancer* **88**(7), 1663–1670 (2000).
33. W. J. Choi, Y. Li, and R. K. Wang, "Monitoring acute stroke progression: multi-parametric OCT imaging of cortical perfusion, flow, and tissue scattering in a mouse model of permanent focal ischemia," *IEEE Trans. Med. Imaging* **38**(6), 1427–1437 (2019).
34. C. L. R. Rodriguez et al., "Decreased light attenuation in cerebral cortex during cerebral edema detected using optical coherence tomography," *Neurophotonics* **1**(2), 025004 (2014).
35. L. Park, H. Young, and K. P. Chan, "Structure-function relationship and diagnostic value of RNFL area index compared with circumpapillary RNFL thickness by spectral-domain OCT," *J. Glaucoma* **22**(2), 88–97 (2013).
36. M. E. Pons et al., "Assessment of retinal nerve fiber layer internal reflectivity in eyes with and without glaucoma using optical coherence tomography," *Arch. Ophthalmol.* **118**(8), 1044–1047 (2000).
37. H. A. Quigley, E. M. Addicks, and W. R. Green, "Optic nerve damage in human glaucoma: III. Quantitative correlation of nerve fiber loss and visual field defect in glaucoma, ischemic neuropathy, papilledema, and toxic neuropathy," *JAMA Ophthalmol.* **100**(1), 135–146 (1982).
38. X.-R. Huang et al., "Reflectance decreases before thickness changes in the retinal nerve fiber layer in glaucomatous retinas," *Invest. Ophthalmol. Visual Sci.* **52**(9), 6737–6742 (2011).
39. X.-R. Huang, R. W. Knighton, and L. N. Cavuoto, "Microtubule contribution to the reflectance of the retinal nerve fiber layer," *Invest. Ophthalmol. Visual Sci.* **47**(12), 5363–5367 (2006).
40. X.-R. Huang et al., "Reflectance spectrum and birefringence of the retinal nerve fiber layer with hypertensive damage of axonal cytoskeleton," *Invest. Ophthalmol. Visual Sci.* **58**(4), 2118–2129 (2017).
41. M. Cianfrocca, "Prognostic and predictive factors in early-stage breast cancer," *Oncologist* **9**(6), 606–616 (2004).
42. U. Veronesi et al., "Sentinel lymph node biopsy in breast cancer: ten-year results of a randomized controlled study," *Ann. Surg.* **251**(4), 595–600 (2010).
43. J. A. Petrek et al., "Lymphedema in a cohort of breast carcinoma survivors 20 years after diagnosis," *Cancer* **92**, 1368–1377 (2001).
44. Y. Jung, Z. Zhi, and R. K. Wang, "Three-dimensional optical imaging of microvascular networks within intact lymph node *in vivo*," *J. Biomed. Opt.* **15**(5), 050501 (2010).
45. R. A. McLaughlin et al., "Imaging of human lymph nodes using optical coherence tomography: potential for staging cancer," *Cancer Res.* **70**(7), 2579–2584 (2010).
46. J. A. Witjes, D. O. T. M. Melissen, and L. A. L. M. Kiemeney, "Current practice in the management of superficial bladder cancer in the Netherlands and Belgian Flanders: a survey," *Eur. Urol.* **49**(3), 478–484 (2006).
47. T. Xie, M. Zeidel, and Y. Pan, "Detection of tumorigenesis in urinary bladder with optical coherence tomography: optical characterization of morphological changes," *Opt. Express* **10**, 1431–1443 (2002).
48. F. J. van der Meer et al., "Apoptosis- and necrosis-induced changes in light attenuation measured by optical coherence tomography," *Lasers Med. Sci.* **25**, 259–267 (2010).
49. R. Engers, "Reproducibility and reliability of tumor grading in urological neoplasms," *World J. Urol.* **25**(6), 595–605 (2007).
50. M. T. J. Bus et al., "Optical coherence tomography as a tool for in vivo staging and grading of upper urinary tract urothelial carcinoma: a study of diagnostic accuracy," *J. Urol.* **196**(6), 1749–1755 (2016).
51. J. E. Freund et al., "Grading upper tract urothelial carcinoma with the attenuation coefficient of in-vivo optical coherence tomography," *Lasers Surg. Med.* **51**, 399–406 (2019).
52. L. P. Hariri et al., "Endoscopic optical coherence tomography and laser-induced fluorescence spectroscopy in a murine colon cancer model," *Lasers Surg. Med.* **38**(4), 305–313 (2006).
53. Y. Furuya and T. Ogata, "Scanning electron microscopic study of the collagen networks of the normal mucosa, hyperplastic polyps, tubular adenoma, and adenocarcinoma of the human large intestine," *Tohoku J. Exp. Med.* **169**(1), 1–19 (1993).
54. J.-F. Toussaint et al., "Water diffusion properties of human atherosclerosis and thrombosis measured by pulse field gradient nuclear magnetic resonance," *Arterioscler. Thromb. Vasc. Biol.* **17**(3), 542–546 (1997).
55. V. Backman et al., "Detection of preinvasive cancer cells," *Nature* **406**(6791), 35–36 (2000).
56. P. G. K. Wagstaff et al., "Percutaneous needle based optical coherence tomography for the differentiation of renal masses: a pilot cohort," *J. Urol.* **195**(5), 1578–1585 (2016).
57. A. Volpe et al., "Contemporary management of small renal masses," *Eur. Urol.* **60**(3), 501–515 (2011).
58. D. Arifler et al., "Light scattering from collagen fiber networks: micro-optical properties of normal and neoplastic stroma," *Biophys. J.* **92**(9), 3260–3274 (2007).
59. A. Swaan et al., "One-to-one registration of en-face optical coherence tomography attenuation coefficients with histology of a prostatectomy specimen," *J. Biophotonics* **12**, e201800274 (2018).
60. G. E. Keles, K. R. Lamborn, and M. S. Berger, "Low-grade hemispheric gliomas in adults: a critical review of extent of resection as a factor influencing outcome," *J. Neurosurg.* **95**(5), 735–745 (2001).
61. E. B. Kiseleva et al., "Optical coefficients as tools for increasing the optical coherence tomography contrast for normal brain visualization and glioblastoma detection," *Neurophotonics* **6**(3), 035003 (2019).
62. C. Kut et al., "Detection of human brain cancer infiltration ex vivo and in vivo using quantitative optical coherence tomography," *Sci. Transl. Med.* **7**(292), 292ra100 (2015).

63. W. Yuan et al., "Robust and fast characterization of OCT-based optical attenuation using a novel frequency-domain algorithm for brain cancer detection," *Sci. Rep.* **7**, 44909 (2017).
64. V. J. Srinivasan et al., "Multiparametric, longitudinal optical coherence tomography imaging reveals acute injury and chronic recovery in experimental ischemic stroke," *PLoS One* **8**(8), e71478 (2013).
65. H. M. Bramlett and W. D. Dietrich, "Pathophysiology of cerebral ischemia and brain trauma: similarities and differences," *J. Cereb. Blood Flow Metab.* **24**(2), 133–150 (2004).
66. T. Gerriets et al., "Edema formation in the hyperacute phase of ischemic stroke. Laboratory investigation," *J. Neurosurg.* **111**(5), 1036–1042 (2009).
67. M. Almasian, T. G. van Leeuwen, and D. J. Faber, "OCT amplitude and speckle statistics of discrete random media," *Sci. Rep.* **7**(1), 14873 (2017).
68. C. Xu, P. Carney, and S. Boppart, "Wavelength-dependent scattering in spectroscopic optical coherence tomography," *Opt. Express* **13**(14), 5450–5462 (2005).
69. H. S. Nam and H. Yoo, "Spectroscopic optical coherence tomography: a review of concepts and biomedical applications," *Appl. Spectrosc. Rev.* **53**(2–4), 91–111 (2018).
70. S. L. Jacques, "Optical properties of biological tissues: a review," *Phys. Med. Biol.* **58**(11), R37–R61 (2013).
71. J. L. Sandell and T. C. Zhu, "A review of *in-vivo* optical properties of human tissues and its impact on PDT," *J. Biophotonics* **4**(11–12), 773–787 (2011).
72. C. A. Patil et al., "Combined Raman spectroscopy and optical coherence tomography device for tissue characterization," *Opt. Lett.* **33**(10), 1135–1137 (2008).

Shuang Chang is a graduate student in Department of Biomedical Engineering at Vanderbilt University. She received her BS degree in biomedical engineering from the University of Rochester in 2018.

Audrey K Bowden is the Dorothy J. Wingfield Phillips Chancellor Faculty Fellow and an associate professor of biomedical engineering (BME) and electrical engineering (ECE) at Vanderbilt University. She received her BSE in electrical engineering from Princeton University, her PhD in BME from Duke University. She is a fellow of SPIE and a senior member of the OSA. Her research interests include biomedical optics—particularly optical coherence tomography—microfluidics, and point of care diagnostics.